Tiantian Yin, Xiaofeng Li, Yu Wang*, Linghui He and Xinglong Gong*

Effect of the meso-structure on the strain concentration of carbon-carbon composites with drilling hole

DOI 10.1515/secm-2017-0114
Received April 1, 2017; accepted May 17, 2017; previously published online July 22, 2017

Abstract: In this work, the influence of fiber/matrix meso-structure on the strain concentration of three-dimensional (3D) reinforced carbon-carbon composites with a drilling hole is discussed by experimental and numerical ways. The full-field digital image correlation (DIC) method is adopted to obtain the strain field of the experimental specimens, and the meso-FEM model with the consistent meso-structure of the experimental specimens is established to reveal the main deformation and damage mechanism. The results show that the strain concentration appeared off the location of ±90° hole tips, which is different with homogeneous material. Furthermore, the shear bands are observed and located on the region between the cut fiber yarn and the adjacent uncut one. The peculiarities are found connecting with the meso-structure. Moreover, the damage locations obtained from the meso-model show good agreements with the experimental fracture path, thereby, the analyses are verified.

Keywords: carbon-carbon composites; digital image correlation; drilling hole; meso-structure; strain concentration.

1 Introduction

The drive to achieve high specific modulus and high specific strength under high temperature has propelled carbon-carbon composites to the forefront among the aerospace structure materials [1–4]. For the needs of connection and other designs, the carbon-carbon composite structures may have various holes. The presence of holes in a structure would inevitably cause a high stress gradient at the vicinity of their edges, which can reduce its structure strength [5, 6], leading to the tendency to damage the structure, or even break down.

Lots of researches have focused on the deformation behaviors of the traditional resin and ceramic matrix composites with open holes [7–13]. Most of them ignore the heterogeneity of the fiber/matrix architecture near the holes. According to the Iosipescu shear test on a carbon-carbon composite by Qin et al. [14], the strain field is found being closely related to the local fiber/matrix architecture. For structures with a hole, it would result in the strain fluctuation in the vicinity of the hole and affect the local strain concentration, even the damage and fracture behaviors. Additionally, as the carbon-carbon composite is more brittle than others, the fracture behavior would be more sensitive to the holes because there is no plastic deformation to dissipate the high concentrated stress around the notches or holes [15–17]. In short, for the research on the mechanical behavior of the carbon-carbon composite with a hole, the complexity of the local behaviors arises from their specific features like heterogeneity, anisotropy. As the motivation for using carbon-carbon composite materials in aerospace structures is increasing, it is necessary to gain a more sufficient understanding of the highly localized strain redistribution around the hole and its influence factor on damage mechanism.

In the current paper, we present results from the experimental and numerical investigation of the local strain fluctuation and the damage features caused by the open hole in the carbon-carbon composite. The full-field digital image correlation (DIC) method [14, 18] is used for displacement, and the strain measurement and results are described. In addition to the experimental investigation, a numerical effort is conducted to match the meso-structures of the experimental specimens. In comparison with the experimental results, the adequacy of the numerical approach is evaluated.

***Corresponding authors: Yu Wang and Xinglong Gong,** Department of Modern Mechanics, CAS Key Laboratory of Mechanical Behavior and Design of Materials, University of Science and Technology of China, Hefei 230027, China, e-mail: wyu@ustc.edu.cn (Y. Wang); gongxl@ustc.edu.cn (X. Gong)
Tiantian Yin, Xiaofeng Li and Linghui He: Department of Modern Mechanics, CAS Key Laboratory of Mechanical Behavior and Design of Materials, University of Science and Technology of China, Hefei 230027, China

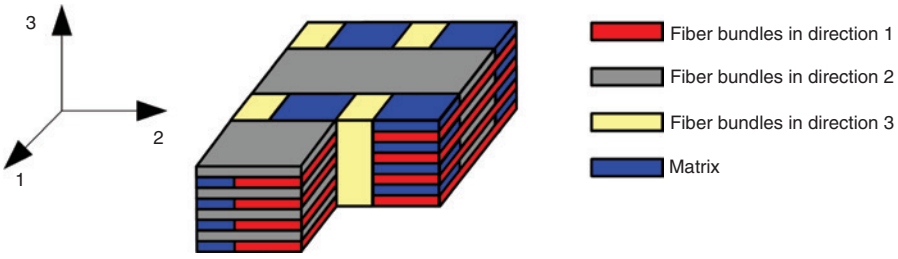

Figure 1: Architecture of 3D carbon-carbon composites.

2 Materials and methods

The architecture of the three-dimensional (3D) orthogonal carbon-carbon composite discussed in this study is shown in Figure 1. The materials are fabricated by the liquid phase infiltration process. The carbon fiber T300 bundles are mutual orthogonal in material directions 1, 2, and 3, which are defined as 1-yarns, 2-yarns, and 3-yarns, respectively. The 1- and 2-yarn fiber bundles are orthogonally laid in one-by-one ply. Then, the 3-yarns fill the 1- and 2-yarn plane in through-thickness direction. At last, the 3D orthogonal architectures are filled by the pitch and carbonized in high temperature. The composites are composed of a lot of periodic units, the unit cell dimension in-plane is approximately 2 mm, and the ply thickness is about 0.25 mm.

Four kinds of specimens with different center holes and one specimen without a hole are tested in the tension experiments. All the specimens are cut in the material plains 1–2. The specimen geometry is shown in Figure 2, where *x* and *y* are in the material directions 1 and 2, respectively. The purpose of these tests is to study the influence of the local meso-structure of fiber/matrix on the local strain distribution around the hole in a carbon-carbon composite.

According to the classical elastic theory, the stress as well as the strain concentration of an isotropic material with a hole can be analytically predicted. The locations are at the ±90° hole tips (the ±90° are with respect to the loading direction), and the strain concentration factor is 3 for the plates with infinite size. However, it is not so easy to determine it for the composite structure, due to its specific features, such as heterogeneity and anisotropy. According to the result of the tension and shear test on carbon-carbon composites without holes by Qin [19], the strain field in the test region would deform nonuniformly and present a periodical distribution. Local in-plane fiber architecture would heavily affect the strain distribution around the hole, especially the strain concentration. Therefore, we choose four specimens with different meso-structures to conduct the experiments. To study the influence of the truncation of the 1-yarn fiber bundles on the strain distribution along the hole, we choose two different types of radius for the experiments. In the 1# and 2# specimens, the circle diameter is 6.8 mm with three and a half 1-yarn fiber bundles cut. For the 3# and 4# specimens, the diameter is 8.6 mm with four 1-yarn fiber bundles cut. About the influence of the truncation of the 2-yarn fiber bundles on the strain concentration around the hole, we design two different kinds of specimens. The 1# and 3# specimens have the 2-yarn fiber bundles arranged along the hole tips, while the 2# and 4# specimens have not. The holes are drilled by wire-electrode cutting. The local meso-structures around the hole for the drilled specimens are illustrated in Figure 3.

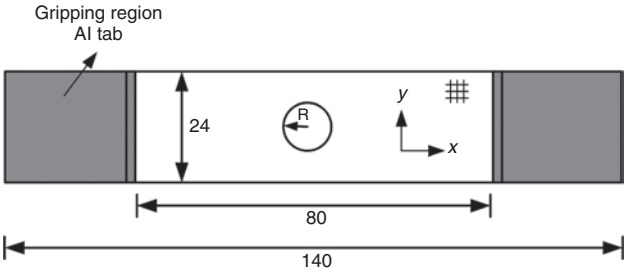

Figure 2: Specimen geometry.

To avoid premature failure in the griping regions, aluminum tabs with 30 mm in length and 2 mm in thickness are adhered to the specimen at both ends with a binder. The tensile tests are conducted on the MTS 809 universal testing machine with a 25-kN load sensor and a constant cross-head speed of 0.05 mm/min.

The DIC method is used as the deformation measurement, as it can obtain both the global and local deformation information of the specimen. The DIC method has been increasingly employed in the work for full-field deformation and strain measurements of the 2D and 3D composite materials [14, 18]. The displacement of any

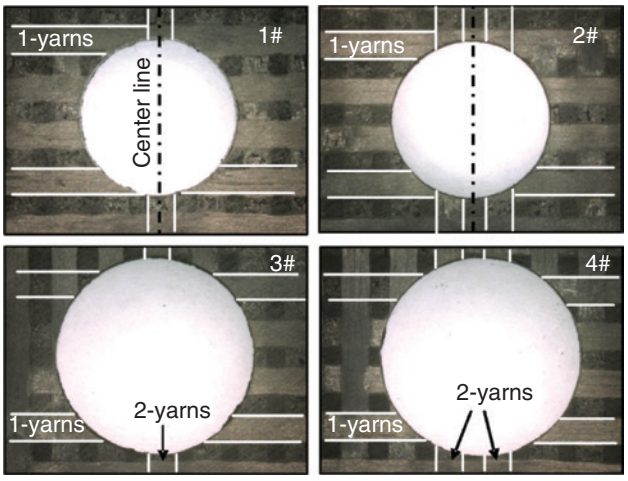

Figure 3: The local meso-structure around the drilling hole.

point on the specimen can be calculated by correlating the two surface feature images of the object before and after deformation. The error of the displacement is about 0.01 ~ 0.05 pixel, which means that the precision can reach 0.2 ~ 1.0 μm. More details of the DIC method can be found in the review of Pan et al. [20]. In this study, the Newton-Raphson sub-pixel search method [21] is adopted. The sub-image size is 45 × 45 pixels, and the step size is 5 × 5 pixels. In order to obtain the more accurate strain fields, a local quadratic fitting smoothing method is used to smooth the displacement field. The smoothing window is 9 × 9 pixels.

Before the experiment, the random speckles are sprayed on the specimen surface with the white and black paint. Meanwhile, we take many measures to guarantee the quality of the speckles, such as adjusting the distance between the spray nozzle and the surface of the test sample. Several pre-experiments are performed to make sure that our speckles are suitable and reliable [21]. When the loading is applied, the experimental images are recorded by a CCD camera simultaneously, which is located in front of the specimen, and the specimen is illuminated by the white light source. The resolution of the CCD camera is 1280 × 960 pixels.

3 Experimental results and discussion

The uniaxial tension experiments of the four different kinds of drilled specimens are performed, and the normal strain $\varepsilon_{11}p$ and the shear engineering strain γ_{12} are obtained by the DIC method. Figure 4 shows the strain contours under the remote strain of 500 με. In order to illustrate the relationship between the strain distribution and the fiber meso-structures around the hole, the fiber bundles in the 1 and 2 directions are plotted in the contours as solid lines and dash lines, respectively.

From the distribution results of the normal strain ε_{11} (Figure 4A), it is found that the normal strain concentration is different with homogenous materials. As we all know, based on the homogenous material assumption, the stress (strain) concentration location is at ±90° hole tips. For isotropic infinite plate containing a hole, the strain concentration factor ($K\varepsilon$) is 3, and for anisotropic material, it is related to the material properties. Based on the material constants by Qin [19], $K\varepsilon$ of the carbon-carbon composite is calculated as 6.9. The strain distributions along the edge of the hole for the different specimens are plotted in Figure 5, in which the strain ratios $\varepsilon_{11}/\varepsilon_{\text{remote}} = 6.9$ are marked. The strain ratios at the −90° position are 2.4, 2.7, 1.1, 0.9, and at the 90° position, they are 1.8, 1.7, 1.4, 1.2 for the 1–4# specimens, respectively. The values are much lower than 6.9. In Figures 4A and 5, it is found that the strain concentration locations of the heterogeneous carbon-carbon composites is away from the hole tips. For the 1# and 2# specimens, the strain in the range of −100° ~ −70° and 70° ~ 100° is obviously higher than the other position, and the strain level is larger in the neighborhood of the 90° hole tip compared to that of the −90° hole tip. As can be seen in Figure 3, as the 1-yarn fiber bundles are only cut in half in the 90° location for the 1# and 2# specimens, the strain field at the bottom of the hole is larger than that at the top. For the 3# and 4# specimens, there exists an obvious strain concentration status along the edge of the hole. The local strain peaks appear at the points of −124°, −57°, 52°, 123° for the 3# and −125°, −57°, 52°, 113° for the 4# specimens. The strain peaks are approximately symmetrical with respect to the central lines drawn in Figure 3.

The shear strain distribution is a bit different from the normal strain. As shown in Figure 4B, there are four obvious shear bands around the hole, which is similar with others [7, 22]. As can be seen in Figure 4B, the shear bands are located between the cut 1-yarn bundles and the uncut one. Because of the cut of the 1-yarn bundles, the load is shifted to the other uncut bundles. According to the shear lag model [23, 24], the local strain field is nonlinear, and there would be a larger shear strain concentration near the cut fiber. The influence of the cut fiber would decay with the increase in distance. As seen in Figures 4B and 5B, the absolute value of the shear strain is largest at −63° and −66° for specimens 1#

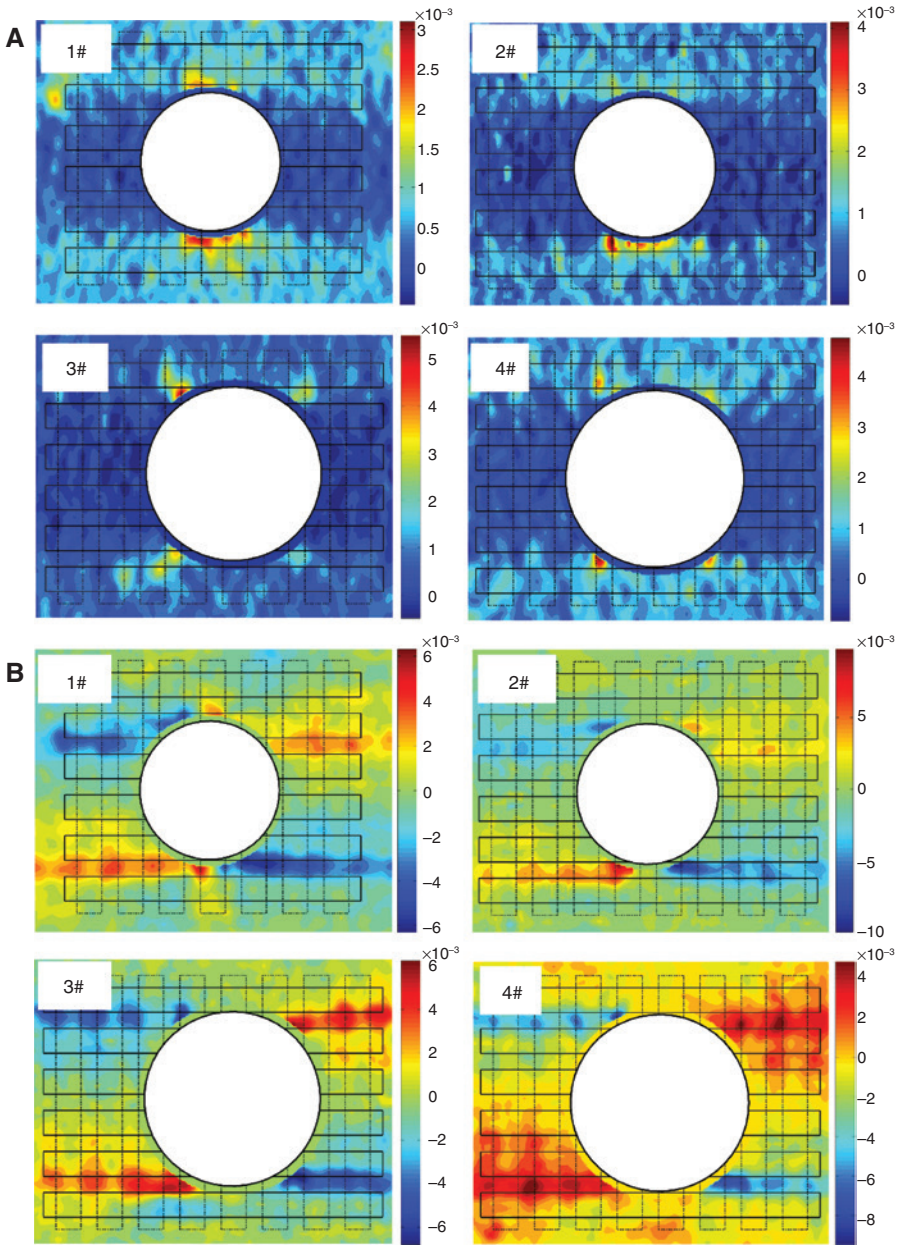

Figure 4: (A) Normal strain distribution in loading direction ε_{11}. (B) Shear strain distribution γ_{12} (solid lines for 1-direction fiber yarns and dash lines for 2-direction yarns).

and 2# and at −55° and −55° for specimens 3# and 4#, respectively.

As Figures 4 and 5 show, whether the 2-yarns are along the 90° or not does not affect the strain concentration significantly. However, the cut of the 1-yarn fiber bundles would affect the symmetry and the strain concentration position around the hole.

As can be clearly observed in Figure 4, a large strain appears in regions between two adjacent 1-yarns or two adjacent 2-yarns, which is mainly matrix material. In general, the carbon matrix has lower stiffness and failure strain compared with the fiber yarn. With loading arising, the matrix may begin to be damaged first. Although it is difficult to observe the micro-cracks using the DIC method, the strain response with different loads can also illustrate the existence of damage.

The normalized ε_{11} along the edge of a hole under different tension loads, 30 MPa, 60 MPa, and 90 MPa, are plotted in Figure 6. All the strain around the peak of the curve is above 0.1%, which is the critical value for damage initiation [19]. It means that around the strain concentration region, the damages have existed along the hole, and

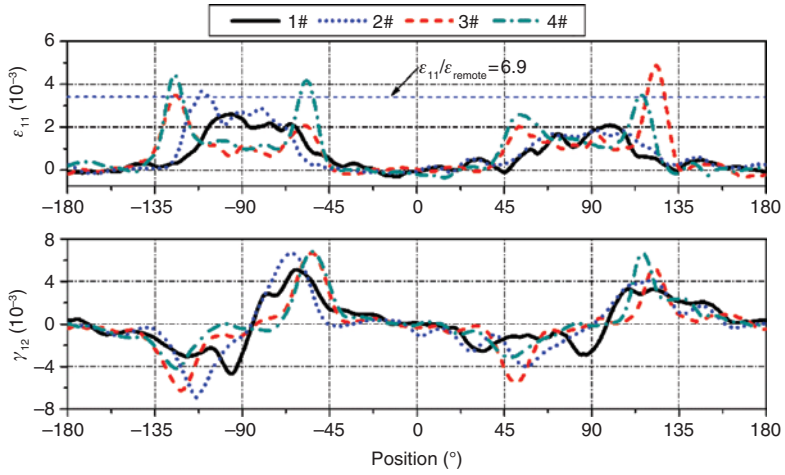

Figure 5: Strain distribution along the edge of the hole for different specimens.

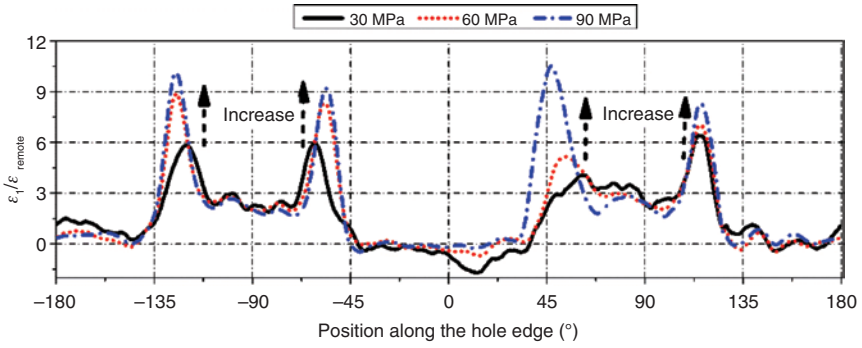

Figure 6: Normalized strain distribution along the edge of the hole under various applied stress (specimen 4#).

it makes the local nonlinear effect present in that region. As a result, the strain does not change with the applied stress linearly anymore. Also, the appearance of damage would result in the redistribution of local stress, which causes the slight shift in the strain concentration, as seen in Figure 6.

As seen from the final failure patterns for different specimens in Figure 7, every specimen presents an obvious brittle fracture behavior accompanied with local fibers pulled out and ply splitting failure occurring in some position. The crack initiation point around the hole coincides with the strain concentration point described above. As mentioned before, damage may initiate from the strain concentration location when the strain reaches the critical value. Then, the damage would gradually propagate through the whole section with load increasing. Meanwhile, from the phenomenon of the fiber pulled out and ply splitting failure, it can be concluded that the interface strength between the fiber and matrix and the interlayer strength has important effects on the damage mechanism of the carbon-carbon composite, which needs further research to work on it.

4 Numerical models

The 3D meso-FEM models are established to help understanding the strain characteristic around the edge of the hole. According to the experiment results, the in-plane meso-structures significantly affect the strain distribution around the hole, and the 3-yarn fibers are ignored in the model. The meso-structure around the hole for the simulated specimens is the same as the experiment ones. The 0° ply and 90° ply are orthogonally laid one-by-one ply, and 12 plies are adopted. The fiber and matrix interface is assumed to have perfect bonding. We adopted the element type of the C3D8 in the commercial software ABAQUS. The number of elements is 287364 for the 1# specimen, 290076 for the 2# specimen, 280224 for the 3# specimen, and

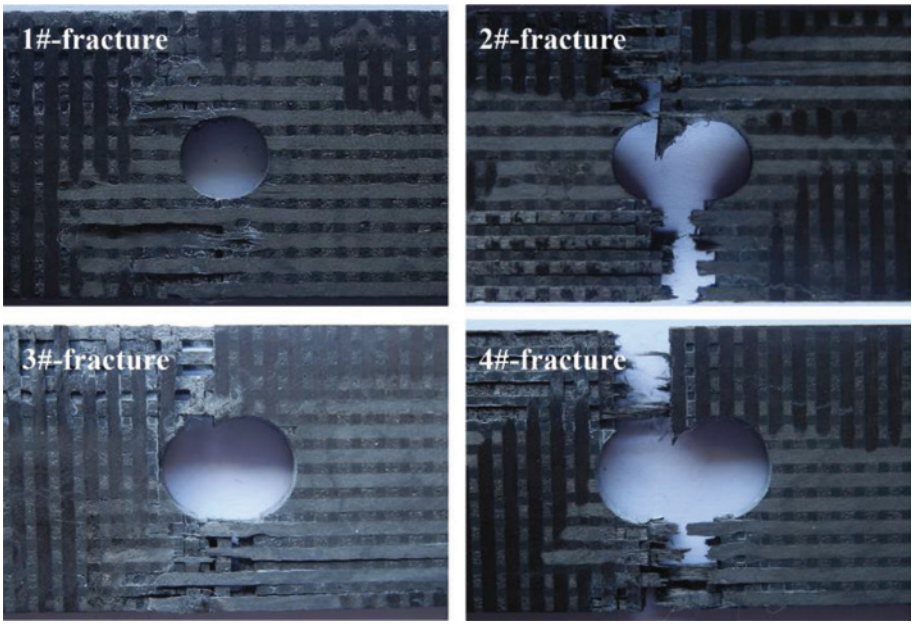

Figure 7: The final fracture patterns of different specimens.

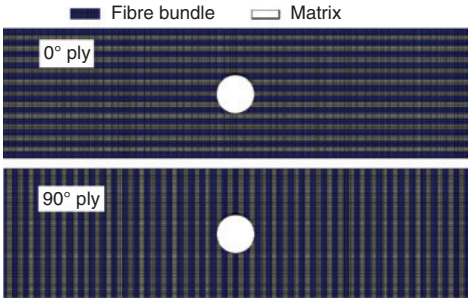

Figure 8: Meso-model of the 1#specimen.

239040 for the 4# specimen. The meso-structures for the 0° ply and the 90° ply of the 1# specimen are illustrated in the Figure 8.

Each fiber bundle consists of much single fibers. Because of restricted calculation resources, it is impossible to consider these constituents within the model. Instead, the model is built up on the yarn scale, considering the fiber bundles as homogeneous with fiber bundle properties. The carbon fiber yarn shows orthotropic behavior and, the mechanical properties are found from the literature data [10] and listed in Table 1, where 1-direction refers to the fiber direction. The carbon matrix is shown in isotropic and the elastic constants Young's modulus E, Poisson's ratio μ, and the shear modulus G are deduced from the experimental data and listed in Table 1.

To model the damage evolution of fiber yarn and matrix, the progressive failure models is adopted, which consists of a stress analysis and a failure analysis [25–27]. The analysis includes failure initiation and evolution. Damage initiation at the presence of a complex stress state can be determined using a failure criterion [28]. The maximum strain criterion is used for fiber bundles and matrix in the following form:

$$\sqrt{\varepsilon_1^2} \geq \varepsilon_1^C \tag{1}$$

where ε_1^C is the maximum failure strain in the longitude direction. In this study, ε_1^C is chosen as 0.254% for fiber bundles, which is obtained by the tensile test of unnotched carbon-carbon composites and as 0.1% for the matrix according to the work of Qin et al. [14].

Once the above criterion is fulfilled, the material will begin to generate failure, and the effective stiff in

Table 1: Elastic constants for each component.

Material type	E_1 (GPa)	$E_2=E_3$ (GPa)	$\mu_{12}=\mu_{13}$	μ_{12}	$G_{12}=G_{13}$ (GPa)	G_{23} (GPa)
Fiber yarn	220.69	13.79	0.2	0.25	8.97	4.83
Matrix	10		0.35		3.7	

direction 1, C_{11}^{d}, is reduced to $(1-d)C_{11,}$ in which C_{11} is the undamaged stiffness, and d is the damage variable, which is given in Eq. (2).

$$d = 1 - \frac{\varepsilon_1^C}{\varepsilon_1} \exp\left(-C_{11} \frac{\varepsilon_1^C}{\varepsilon_1} (\varepsilon_1 - \varepsilon_1^C) L^c / G_t \right) \tag{2}$$

where L^c is the characteristic length associated with the material point of the element. G_t is the fracture energy per unit area, which is a key parameter to control gradual degradation of a material, and the values of the fiber yarns and matrix are assumed to be 12 N/mm and 1 N/mm, respectively [26]. It is obvious that d is between 0 and 1, and $d=0$ and 1 indicate undamaged and fully damaged status, respectively.

The numerical simulation is carried out by using the commercial FEM software ABAQUS by ABAQUS Inc, Pawtucket, RI, USA. The constitutive equations of the elastic behavior, and the damage initiation and evolution are defined in the user subroutine program UMAT [27]. Based on the above model, the strain distribution around the hole and the damage evolution process are analyzed.

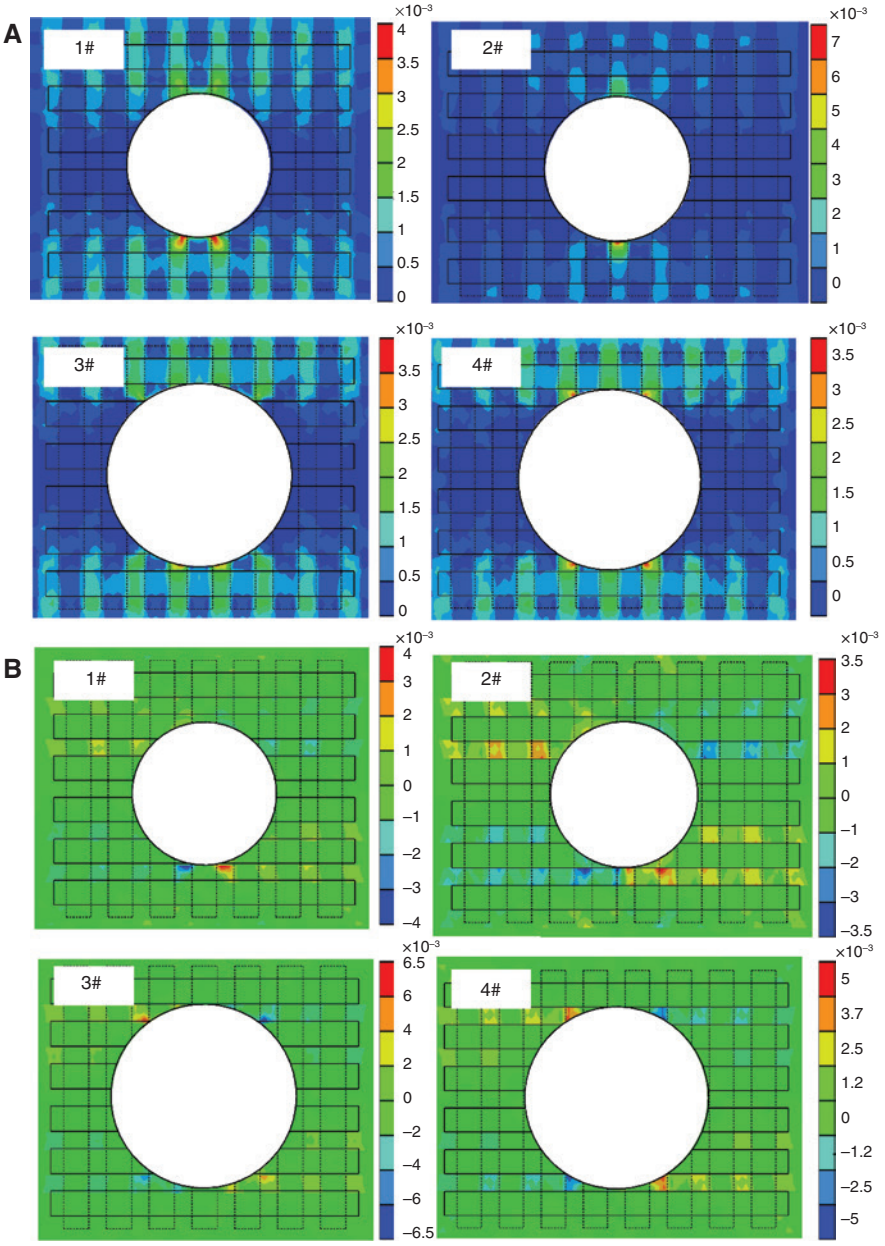

Figure 9: Simulated strain distribution (A) ε_{11} and (B) γ_{12} of 0° ply (solid lines for 1-direction fiber yarn and dash lines for 2-direction yarn).

5 Numerical analysis and discussion

As from the simulation results, the 0° ply bears most of the load, and the strain concentration around the hole is more serious than that of the 90° ply. Here, only the results of the 0° ply are discussed. The calculated normal strain ε_{11} and shear strain γ_{12} contours by the meso-model are shown in Figure 9. The fiber yarn meso-structures are also marked in the figure as in the experimental results. The strain distributions by the models along the edge of the hole are plotted in Figure 10.

As shown in Figures 9 and 10, the strain distribution is found being related to the meso-structure, and the strain is symmetrical with respect to the central lines. As can be seen clearly, the relatively larger strain occurs at the region between two adjacent fibers yarns, which is a matrix material. For convenience in describing, the regions between two adjacent 1-yarn fiber and the regions between two adjacent 2-yarns are defined as region-1 and region-2.

From the contour of the normal strain, the strain peaks are away from ±90° and are located in the cross region of region-1 and region-2 along the edge of the hole, which is more regular than the experimental results. The normal strain of the 1# specimen, as shown in Figure 9A, concentrates at the first cross area of region-1 and region-2 from the −90° hole tip at the hole edge, and the larger platform strain near the 90° hole tip exists in the range of 70° ~ 100°. The results match well with the experiment one. The normal strains for 1# and 2# are larger in the adjacency of the −90° hole tip compared to that of the 90° hole tip, the same as the experimental results. The reason comes from the half cut 1-yarn fibers in the 90° hole tip for the 1# and 2# specimens. They can still bear the load and reduce the strain concentration in the 90° position, which also can be taken from the simulation results. For the 2# and 3# specimens, the distributions of the simulated normal strain are a little different from the experiment one, which may be caused by the small defects in the experiment specimens induced by the drilling operation and need to be confirmed by further research. The normal strain peaks of the 4# specimen agree well with experimental results and are also symmetrical about the central axis.

The shear strain distribution of the numerical model is demonstrated in Figure 9B. The positions of the simulated shear bands agree well with the experimental data, and the shear bands are found on region-2. In addition, as can be seen in Figure 10, the larger shear bands are located at the region between the cut 1-yarn bundles and the uncut one, which is related as region-1 here.

Figure 11 is the damage result based on the damage model discussed in Section 4. The initial damage occurs in the matrix material, and the positions appear at the strain concentration point discussed previously. Then, the fiber materials, which are located near the damaged matrix, begin to generate damage. The simulated damage propagation path is found coinciding with the experimental fracture path marked with arrows. As no proper fiber pulled out and ply splitting failure model is considered in

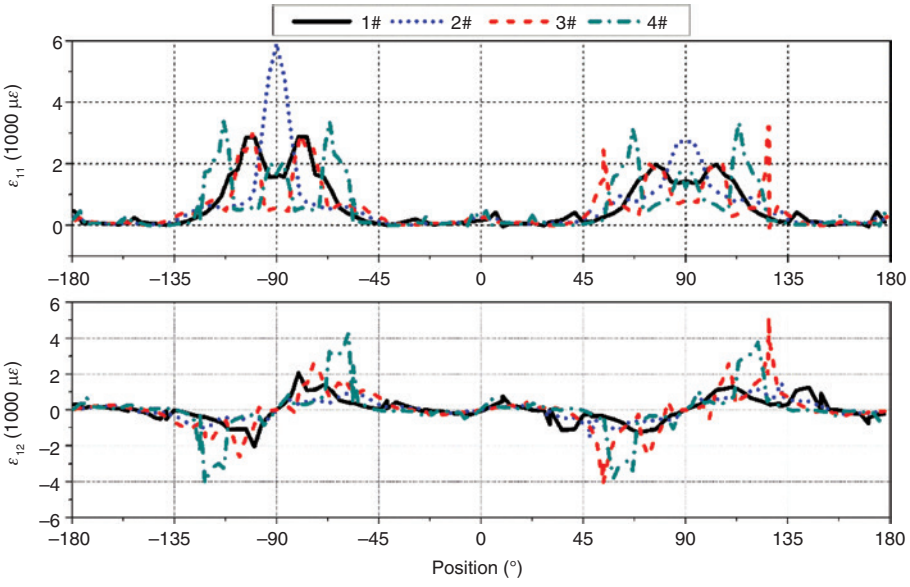

Figure 10: Strain distribution along the edge of the hole obtained from meso-models.

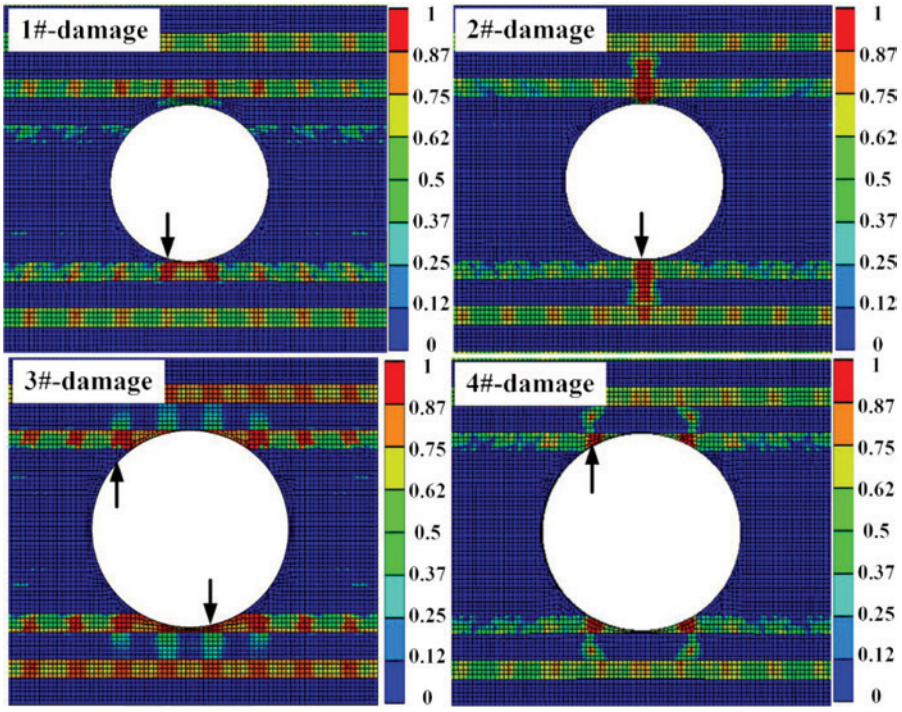

Figure 11: Damage variable distribution.

the numerical model, no fiber pulled out and ply splitting failure phenomena are reported in the simulation results.

6 Conclusion

By using the full-field measurement DIC method, the strain distribution of the holed 3D carbon-carbon composites is obtained. The strain field associated with the meso-structures in the vicinity of the hole is clearly observed. The strain concentration positions are away from the ±90° hole tip location. Where 1-yarns at ±90° are cut is found having significant effect on the symmetry and the strain concentration, while the influence of the 2-yarns is not so significant. The shear strain bands are also observed, and the larger shear strain zone is located between the cut 1-yarn fibers and the adjacent uncut one. Furthermore, by the meso-model, the characteristic of the strain distribution is obtained and compared with the experimental results. It shows that the strain concentration is symmetrical about the axis if the meso-structure is symmetrical about the axis. If the 1-yarns are half cut at one side along the hole, the strain symmetrical characteristic will be broken. According to the damage analysis, the initial location of the damaged path is related to the strain concentration position. In addition, further research work needs to be done on the proper parameters to better describe the fiber pulled out and ply splitting failure phenomena observed in some experiments.

Acknowledgments: Financial support from the National Natural Science Foundation of China (Grant No. 11372301), the Fundamental Research Funds for the Central Universities (WK2480000002), and the Strategic Priority Research Program of the Chinese Academy of Sciences (Grant No. XDB22040502) are gratefully acknowledged. This work is also supported by the Collaborative Innovation Center of Suzhou Nano Science and Technology.

References

[1] Chen ZK, Xiang X, Li GD, Wang YL. *J. Mater. Sci.* 2010, 45, 3477–3482.
[2] He YG, Li KZ, Li HJ, Wei JF, Fu QG, Zhang DS. *J. Mater. Sci.* 2010, 45, 1432–1437.
[3] You LH. *Sci. Eng. Compos. Mater.* 2002, 10, 297–312.
[4] Ozcan S, Tezcan J, Gurung B, Filip P. *J. Mater. Sci.* 2010, 46, 38–46.
[5] Yang Z, Kim C, Cho C, Beom HG. Int. *J. Solids Struct.* 2008, 45, 713–731.
[6] Toubal L, Karama M, Lorrain B. *Compos. Struct.* 2005, 68, 31–36.
[7] Awerbuch J, Madhukar MS. *J. Reinf. Plast. Compos.* 1985, 4, 3–159.
[8] Ghezzo F, Giannini G, Cesari F, Caligiana G. *Compos. Sci. Technol.* 2008, 68, 1057–1072.

[9] Mendoza Jasso AJ, Goodsell JE, Ritchey AJ, Byron Pipes R, Koslowski M. *Compos. Sci. Technol.* 2011, 71, 1819–1825.
[10] Ng SP, Lau KJ, Tse PC. *Compos. Part B* 2000, 31, 113–132.
[11] Pandita SD, Nishiyabu K, Verpoest I. *Compos. Struct.* 2003, 59, 361–368.
[12] Santhosh U, Ahmad J, John R, Ojard G, Miller R, Gowayed Y. *Compos. Part B* 2013, 45, 1156–1163.
[13] Dassios KG, Kordatos EZ, Aggelis DG, Matikas TE. *Sci. World J.* 2013, 2013, 1–12.
[14] Qin LJ, Zhang ZW, Li XF, Yang XG, Feng ZH, Wang Y, Miao H, He L, Gong XL. *Compos. Part A* 2012, 43, 310–316.
[15] He MY, Wu B, Suo Z. *Acta Metall. Mater.* 1994, 42, 3065–3070.
[16] Heredia FE, Mark SS, Mackin TJ, He MY, Evans AG, Mosher P, Brondsted P. *J. Am. Ceram. Soc.* 1994, 77, 2817–2827.
[17] Mackin TJ, Perry KE, Epstein JS, Cady C, Evans AG. *J. Am. Ceram. Soc.* 1996, 79, 65–73.
[18] Wang Z, Li H, Tong J, Shen M, Aymerich F, Priolo P. *Compos. Sci. Technol.* 2008, 68, 1975–1980.
[19] Qin LJ. University of Science and Technology of China; 2013.
[20] Pan B, Qian K, Xie H, Asundi A. *Meas. Sci. Technol.* 2009, 20, 1–17.
[21] Bruck HA, McNeill SR, Sutton MA, Peters WH. *Exp. Mech.* 1989, 29, 261–267.
[22] Hutchinson JW, Tvergaard V. *Int. J. Solids Struct.* 1981, 17, 451–470.
[23] Cox H. *Br. J. Appl. Phys.* 1952, 3, 72–79.
[24] Jiang G, Peters K. *Int. J. Solids Struct.* 2008, 45, 4049–4067.
[25] Huang ZM. *J. Reinf. Plast. Compos.* 2007, 26, 1135–1181.
[26] Shigang A, Daining F, Rujie H, Yongmao P. *Compos. Part B* 2015, 71, 113–121.
[27] ABAQUS Inc, Pawtucket, RI, USA; 2013.
[28] Lubineau G, Ladevèze P. *Compos. Mater. Sci.* 2008, 43, 137–145.